Author's personal copy

International Journal of Heat and Fluid Flow 38 (2012) 94–106

Contents lists available at SciVerse ScienceDirect

International Journal of Heat and Fluid Flow

journal homepage: www.elsevier.com/locate/ijhff

Fully-developed conjugate heat transfer in porous media with uniform heating

D.J. Lopez Penha [a,*], S. Stolz [a], J.G.M. Kuerten [a,c], M. Nordlund [d], A.K. Kuczaj [d], B.J. Geurts [a,b]

[a] Department of Applied Mathematics, University of Twente, P.O. Box 217, 7500 AE Enschede, The Netherlands
[b] Department of Applied Physics, Eindhoven University of Technology, P.O. Box 513, 5600 MB Eindhoven, The Netherlands
[c] Department of Mechanical Engineering, Eindhoven University of Technology, P.O. Box 513, 5600 MB Eindhoven, The Netherlands
[d] Philip Morris International Research & Development, Philip Morris Products S.A., Quai Jeanrenaud 5, 2000 Neuchâtel, Switzerland

ARTICLE INFO

Article history:
Received 25 January 2012
Received in revised form 2 July 2012
Accepted 25 August 2012
Available online 11 October 2012

Keywords:
Porous medium
Incompressible fluid
Conjugate heat transfer
Fully developed flow
Nusselt number
Direct numerical simulation

ABSTRACT

We propose a computational method for approximating the heat transfer coefficient of fully-developed flow in porous media. For a representative elementary volume of the porous medium we develop a transport model subject to periodic boundary conditions that describes incompressible fluid flow through a uniformly heated porous solid. The transport model uses a pair of pore-scale energy equations to describe conjugate heat transfer. With this approach, the effect of solid and fluid material properties, such as volumetric heat capacity and thermal conductivity, on the overall heat transfer coefficient can be investigated. To cope with geometrically complex domains we develop a numerical method for solving the transport equations on a Cartesian grid. The computational method provides a means for approximating the heat transfer coefficient of porous media where the heat generated in the solid varies "slowly" with respect to the space and time scales of the developing fluid. We validate the proposed method by computing the Nusselt number for fully developed laminar flow in tubes of rectangular cross section with uniform wall heat flux. Detailed results on the variation of the Nusselt number with system parameters are presented for two structured models of porous media: an inline and a staggered arrangement of square rods. For these configurations a comparison is made with literature on fully-developed flows with isothermal walls.

© 2012 Elsevier Inc. All rights reserved.

1. Introduction

Porous media are known for their complex network of interconnected pores, which often displays large variations in its length scales (Bear, 1988; Dullien, 1979). Technological applications of porous media specifically exploit this intricate network to, for example, trap particles moving in the fluid (Hinds, 1999) or to enhance the transfer of heat between the fluid and the solid walls (Kaviany, 1995). To optimally design for such technologies it is necessary to have a detailed understanding of the transport properties of mass, momentum and energy in porous media. In this paper we develop a computational method for performing pore-scale (i.e., microscopic) simulations of fluid flow and conjugate heat transfer. We solve transport equations subject to periodic boundary conditions in a representative elementary volume of the porous medium under consideration. Using these detailed results we then compute, in a "first principles" approach, the bulk heat transfer coefficient—as is used in the volume-averaged (i.e., macroscopic) description of energy transport (Kaviany, 1995).

Most practical models for transport phenomena in porous media adopt a macroscopic description of averaged flow quantities, as a full microscopic treatment is computationally too demanding (Brenner and Edwards, 1993). Macroscopic balance equations are derived from their microscopic counterparts using a spatial filtering technique which introduces a "coarsening" length-scale (Whitaker, 1999). This up-scaling technique has the beneficial effect of reducing the overall size of the computational problem by allowing for a description which requires less degrees-of-freedom per unit of physical volume. However, filtering also introduces a closure problem, as several terms in the macroscopic balance equations need to be modeled before a solution can be obtained (Whitaker, 1999). For the macroscopic energy equation in particular, one such important term describes the net rate of heat transfer between the subfilter-scale solid and fluid components (Quintard et al., 1997). It is generally modeled as a simple expression involving the phase-averaged temperatures and a heat transfer coefficient (Quintard et al., 1997; Kuwahara et al., 2001). Finding a suitable value for the heat transfer coefficient is important for an accurate description of macroscopic energy transport, and requires detailed knowledge of the underlying pore structure, flow characteristics, and material properties. To determine the heat transfer coefficient—and similarly for other bulk parameters—microscopic simulations can be performed using a representative elementary volume (REV) that accurately describes the geometry of the porous medium (Kaviany, 1995). Several examples of this detailed

* Corresponding author. Tel.: +31 534894272.
E-mail address: d.j.lopezpenha@utwente.nl (D.J. Lopez Penha).

0142-727X/$ - see front matter © 2012 Elsevier Inc. All rights reserved.
http://dx.doi.org/10.1016/j.ijheatfluidflow.2012.08.007

Author's personal copy

Nomenclature

a	mean gradient of pressure
A_{sf}	solid–fluid interface
c_p	volumetric heat capacity = ρC_p
C_p	specific heat capacity at constant pressure
$\boldsymbol{e}_x$	unit vector along the x-axis
E	total energy
$\boldsymbol{f}$	forcing function for the immersed boundary method
h_{sf}	heat transfer coefficient
L_{ref}	reference length
Nu	Nusselt number = $h_{sf}L_{\mathrm{ref}}/\lambda_f$
$\boldsymbol{n}$	unit normal vector
p	pressure
Pr	Prandtl number = $\nu c_{p,f}/\lambda_f$
q_{sf}	net rate of interphase heat transfer
Q	volumetric heat source
R_{c_p}	volumetric heat capacity ratio = $c_{p,s}/c_{p,f}$
R_λ	thermal conductivity ratio = λ_s/λ_f
Re	Reynolds number = $u_{\mathrm{ref}}L_{\mathrm{ref}}/\nu$
T	temperature
t	time
u, v, w	velocity components in the x, y and z directions
u_{ref}	reference velocity
$\mathcal{V}$	representative elementary volume $= \mathcal{V}_s \cup \mathcal{V}_f$
x, y, z	components of the coordinate axes

Greek symbols

α	mean gradient of temperature
ϵ	relaxation time for the immersed boundary method
Γ	phase-indicator function
λ	thermal conductivity
∇	vector differential operator
ν	kinematic viscosity
ϕ	porosity $= \mathcal{V}_f/\mathcal{V}$
ρ	density

Superscripts and subscripts

$(\,)^*$	dimensionless quantity
$(\tilde{\ })$	periodic variable field
$(\,)_f$	property of the fluid phase
$(\,)_s$	property of the solid phase
$(\,)_{\mathrm{ref}}$	reference quantity
$\langle\rangle_f$	volume average over the fluid phase
$\langle\rangle_s$	volume average over the solid phase
$\langle\rangle^f$	intrinsic volume average over the fluid phase
$\langle\rangle^s$	intrinsic volume average over the solid phase

approach can be found in Quintard et al. (1997), Kuwahara et al. (2001), Nakayama et al. (2002, 2004), and Sahraoui et al. (1994).

An approach to computing the heat transfer coefficient that involves the solution of fundamental equations of transport subject to periodicity constraints on a REV has been presented in Kuwahara et al. (2001). In this approach, a transport model is used to simulate fully-developed flow of an incompressible fluid heated by isothermal walls. This flow corresponds to the physical configuration where the fluid is being heated by a solid with a much higher volumetric heat capacity and thermal conductivity (Tiselj et al., 2001). In this paper we propose an extension to this model to include solid heat conduction, thereby creating a thermal link between the two phases for supporting conjugate heat transfer. By allowing for conjugate heat transfer we allow for a description in which a change in the heat transfer coefficient can now be attributed to a change in the solid and fluid material properties, i.e., the volumetric heat capacity and thermal conductivity. A transport model is developed which simulates hydrodynamically and thermally fully-developed flow in a REV. To solve the transport equations we adopt a numerical solution strategy that uses a generalized immersed boundary method on a Cartesian grid, which greatly simplifies the simulation of heat and fluid flow in geometrically complex domains. The novelty of the proposed transport model and simulation strategy is twofold. Firstly, the proposed transport model integrates conjugate heat transfer in the porous media context using the immersed boundary method. This transport model has not been put into practice except for problems of heat transfer in (turbulent) fully developed wall-bounded channel flow (see, e.g., Tiselj et al., 2001; Bejan, 1993; Incropera and DeWitt, 1990). Secondly, application of the developed simulation strategy allows for the direct computation of the heat transfer coefficient (Nusselt number) of porous media on the basis of the pore-scale flow, and can thus be used for macroscopic, engineering investigations.

We determine the heat transfer coefficient of an incompressible fluid flowing through a uniformly heated porous solid. The governing equations for fluid flow are the incompressible Navier–Stokes equations with a modification to accommodate for "immersed boundaries" (Mittal and Iaccarino, 2005). We use an immersed boundary method by including a source term into the momentum equation to approximate the no-slip condition on the solid–fluid interface (Lopez Penha et al., 2011). This source term allows us to directly enforce the boundary condition through the governing equations (Mittal and Iaccarino, 2005). As a consequence, we can avoid the cumbersome process of generating a body-conforming grid. This technique provides a simple and effective way to approximate the flow of fluid through a geometrically complex domain. For the thermal coupling, we consider a general advection–diffusion equation for the fluid phase and a diffusion equation with a constant volumetric heat source for the solid phase. This heat transfer problem can be interpreted as an idealization of a setting where the heat generated in the solid varies "slowly" with respect to the space and time scales of the developing flow field.

The proposed computational method will be validated by simulating fully developed laminar flow in tubes of constant cross section. Results on the Nusselt number will be compared with various analytical and numerical results from literature for tubes of rectangular cross section. We will demonstrate that the transport model—in the limit of a large, solid phase thermal conductivity—produces fully developed flow at a constant wall heat flux. The numerical method is shown to be, at best, second-order accurate for flow domains where the solid–fluid interface can be aligned with the grid lines of the Cartesian grid. It is otherwise first-order accurate for both the hydro-and thermodynamics.

As an application to porous media, we will simulate fully-developed flow in two structured models of porous media: an infinite array of square rods in an inline and a staggered arrangement. Nusselt number computations will be presented for a range of Reynolds numbers and ratios of the solid-to-fluid thermal conductivity. We will demonstrate that for sufficiently small Reynolds numbers the Nusselt number is constant. By increasing the Reynolds number the Nusselt number will increase monotonically. For the ratio of solid-to-fluid thermal conductivity $R_\lambda < 100$ the Nusselt number varies significantly (while keeping the Reynolds number constant). As for the ratio $R_\lambda \geqslant 100$, the Nusselt number remains constant with a change in R_λ. These changes are all

Author's personal copy

attributed to a shift in the dominant physical mechanisms of heat transfer. We will also compare our results to literature on fully-developed flows with isothermal walls.

This paper is organized as follows: in Section 2 we describe the transport model used for simulating fully-developed flow in porous media. The numerical method for solving the governing transport equations is described in Section 3. In Section 4 we compute the Nusselt number for both the inline and staggered arrangements of square rods. A summary of the results and the conclusions is provided in Section 5. In Appendix B we validate the proposed computational method using rectangular tubes.

2. Periodic model for microscopic heat transport

To understand the bulk behavior of macroscopic energy transport, i.e., the behavior away from entrance or exit areas, we realize a closure of the heat transfer coefficient using a model for microscopic energy transport subject to periodic boundary conditions; hereafter referred to conveniently as the "periodic transport model". In this approximation, we model the porous medium under consideration as an infinite, three-dimensional array, with a *representative elementary volume* (REV) (Bear, 1988; Dullien, 1979) of the porous medium functioning as the repeating pore pattern (see Fig. 1). The characteristic size L of the REV is small compared to the macroscopic size of the full system. It is also considered large compared to the characteristic size of the microscopic structures it contains, as to not have the periodic conditions significantly influence the bulk behavior of the flow. The computational domain $\mathcal{V}$ is taken to be of the same size as the REV and is occupied by a fluid phase $\mathcal{V}_f$ and a solid phase $\mathcal{V}_s$. We simulate in $\mathcal{V}$ fully-developed flow of an incompressible fluid through a uniformly heated porous solid. Using the detailed solution the heat transfer coefficient can then be obtained in terms of the material properties and the flow conditions.

In this section we discuss in detail the periodic transport model. As a starting point we consider the microscopic balance equations for fluid and energy transport in $\mathcal{V}$, and then rewrite them in terms of spatially periodic field variables, i.e., velocity, pressure and temperature. We will assume steady transport, and the direction of forced convection to be solely parallel to the x-axis. All results produced can be generalized to unsteady flows and to arbitrary flow directions.

2.1. Incompressible fluid flow

Consider the motion of an incompressible, Newtonian fluid under a constant volumetric flow rate. This motion is governed by the Navier–Stokes equations (Bird et al., 2002), expressed here in dimensional form:

$$\nabla \cdot \boldsymbol{u} = 0, \tag{1a}$$

$$\frac{\partial \boldsymbol{u}}{\partial t} + \nabla \cdot (\boldsymbol{u}\boldsymbol{u}) = -\nabla p + \nu \nabla \cdot \nabla \boldsymbol{u} + \boldsymbol{f}, \tag{1b}$$

valid for the coordinate $\boldsymbol{x} = (x, y, z)^T \in \mathcal{V}$. The symbols in the equations represent: fluid velocity vector $\boldsymbol{u} = (u, v, w)^T$, pressure $p \equiv P/\rho_f$ divided by the fluid mass-density ρ_f, kinematic viscosity ν, and vector differential operator $\nabla \equiv (\partial/\partial x, \partial/\partial y, \partial/\partial z)^T$. We will use the source term:

$$\boldsymbol{f} \equiv -\frac{1}{\epsilon}\Gamma \boldsymbol{u}, \tag{2}$$

to approximate the no-slip boundary condition, i.e., $\boldsymbol{u} = \boldsymbol{0}$, along the solid–fluid interface, A_{sf}, by "penalizing" the entire domain $\mathcal{V}_s$ (Lopez Penha et al., 2011). It is a way of implementing the boundary condition dynamically through the governing equations, and provides an alternate way of solving a boundary value problem (Mittal and Iaccarino, 2005). Numerically, this approach is convenient for the simulation of flows in complex domains as (1) is now extended to include the solid domain $\mathcal{V}_s$. The positive parameter ϵ can be interpreted as a relaxation time that governs the rate-of-return of $\boldsymbol{u}$ to its equilibrium value of $\boldsymbol{u} = \boldsymbol{0}$ in $\mathcal{V}_s$. $\Gamma(\boldsymbol{x})$ is a binary valued, phase-indicator function, such that: $\Gamma = 0$ for $\boldsymbol{x}$ in the fluid domain and $\Gamma = 1$ for $\boldsymbol{x}$ in the solid domain. For further details on this approach we refer to Lopez Penha et al. (2011).

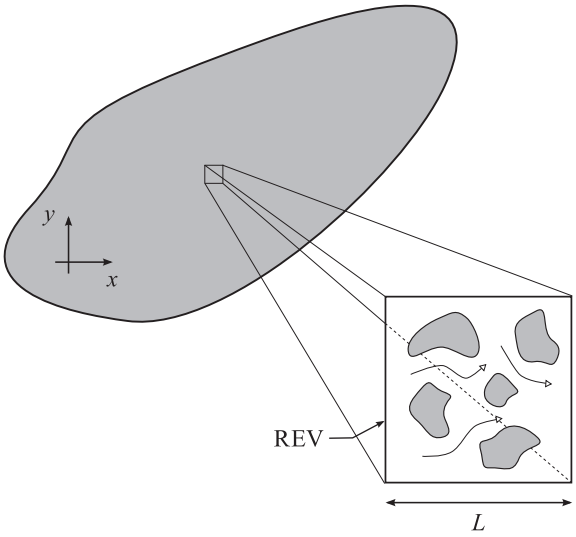

(a) REV of a porous medium.

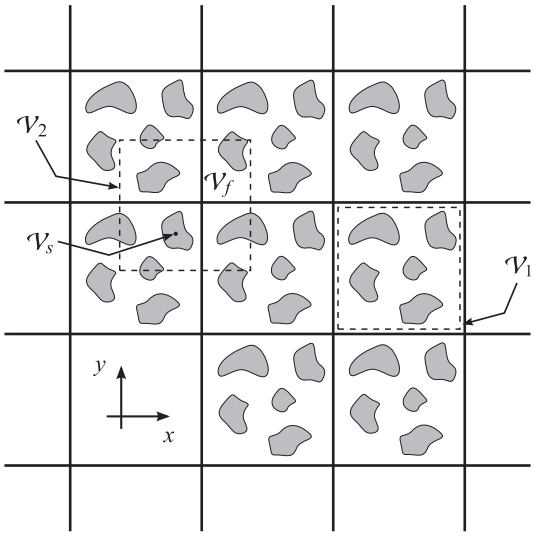

(b) Model porous medium composed of a periodic repetition of REVs.

Fig. 1. Representative elementary volume (REV) of a porous medium with characteristic length L. The infinite array of REVs is used as a model for the porous medium through which fully-developed flow is simulated. The size of the computational domain $\mathcal{V}$ is taken equivalent to that of a single REV, where $\{\mathcal{V}_f, \mathcal{V}_s\}$ represent the total fluid and solid volume inside $\mathcal{V}$, respectively. Volumes $\mathcal{V}_1$ and $\mathcal{V}_2$ are equivalent.

Under the condition of a constant volumetric flow rate coupled with a periodic porous medium, it is commonly assumed that in the fully-developed state the velocity field is spatially periodic (Moin and Kim, 1982). For example, along the x-axis, this results in the condition:

$$\boldsymbol{u}(\boldsymbol{x}) = \boldsymbol{u}(x + kL, y, z), \quad k \in \mathbb{Z}; \tag{3}$$

Author's personal copy

with L the length of $\mathcal{V}$ along the x-axis (see Fig. 1). A similar condition holds for the velocity vector along the y and z axes, each with a period equal to the dimension of $\mathcal{V}$ along their respective direction. The pressure term p is decomposed into a linear component and a spatially periodic component (designated by the tilde):

$$p = ax + \tilde{p}. \tag{4}$$

The value of a, i.e., the mean gradient of pressure in the x-direction, is selected such that the desired flow rate is achieved (Lopez Penha et al., 2011).

All simulations will be performed on dimensionless equations, and we select reference scales for length L_{ref}, velocity u_{ref}, and kinematic viscosity ν. In dimensionless form, (1) is expressed as:

$$\nabla^* \cdot \boldsymbol{u}^* = 0, \tag{5a}$$

$$\frac{\partial \boldsymbol{u}^*}{\partial t^*} + \nabla^* \cdot (\boldsymbol{u}^* \boldsymbol{u}^*) = -(\nabla^* \tilde{p}^* + a^* \boldsymbol{e}_x) + \frac{1}{\text{Re}} \nabla^* \cdot \nabla^* \boldsymbol{u}^* - \frac{1}{\epsilon^*} \Gamma \boldsymbol{u}^*, \tag{5b}$$

where the asterisk is used to designate dimensionless quantities. Eq. (5) represents a periodic model for fluid transport. The Reynolds number is defined as $\text{Re} = u_{\text{ref}} L_{\text{ref}}/\nu$, and the unit vector in the direction of the x^*-axis is represented by $\boldsymbol{e}_x \equiv (1,0,0)^T$. We solve (5), for $\{\boldsymbol{u}^*, \tilde{p}^*\}$, in time until a steady state is achieved, at which point the flow is hydrodynamically fully developed.

2.2. Conjugate heat transfer

Consider the two-way transfer of heat between the solid and the fluid domain, where the solid is being heated throughout by a constant source of energy. The governing energy equations, written with respect to temperature T, are given in their dimensional form by (Bird et al., 2002):

$$c_{p,f} \frac{\partial T_f}{\partial t} + \nabla \cdot (\boldsymbol{u} c_{p,f} T_f) = \nabla \cdot (\lambda_f \nabla T_f) \quad \text{for} \quad \boldsymbol{x} \in \mathcal{V}_f, \tag{6a}$$

$$c_{p,s} \frac{\partial T_s}{\partial t} = \nabla \cdot (\lambda_s \nabla T_s) + Q \quad \text{for} \quad \boldsymbol{x} \in \mathcal{V}_s; \tag{6b}$$

where the subscripts $\{f, s\}$ designate fluid and solid properties, respectively. As for the remaining symbols: $c_p \equiv \rho C_p$ is the volumetric heat capacity, C_p is the specific heat capacity at constant pressure, λ is the thermal conductivity, and Q is a constant volumetric heat source. All material properties are assumed constant within each phase. Along the solid–fluid interface A_{sf}, the following conditions for *continuity of temperature* and *continuity of heat flux* are effective at all times t:

$$T_f = T_s \quad \text{and} \quad \lambda_f \nabla T_f \cdot \boldsymbol{n}_{fs} = \lambda_s \nabla T_s \cdot \boldsymbol{n}_{fs}, \tag{7}$$

with $\boldsymbol{n}_{fs}$ the unit outwardly directed normal away from the fluid phase.

To apply streamwise periodicity, we—in a similar treatment as for p—separate the periodic component of T such that (Lu and Hetsroni, 1995):

$$T_f = \alpha x + \widetilde{T}_f \quad \text{and} \quad T_s = \alpha x + \widetilde{T}_s; \tag{8}$$

where $\{\widetilde{T}_f, \widetilde{T}_s\}$ represent the periodic components. The mean gradient of temperature, α, is given by:

$$\alpha = \frac{(1-\phi)Q}{c_{p,f}\langle u \rangle_f}, \tag{9}$$

where $\phi \equiv \mathcal{V}_f/\mathcal{V}$ is the porosity and $\langle u \rangle_f$ is the average velocity in $\mathcal{V}$ [refer to Eq. (A.4)]. Eq. (9) is determined by performing a balance of energy in $\mathcal{V}$ (see Appendix A). Substituting the decompositions into (6), a periodic model for energy transport is obtained:

$$c_{p,f} \frac{\partial \widetilde{T}_f}{\partial t} + \nabla \cdot (\boldsymbol{u} c_{p,f} \widetilde{T}_f) = \nabla \cdot (\lambda_f \nabla \widetilde{T}_f) - \alpha u c_{p,f}, \tag{10a}$$

$$c_{p,s} \frac{\partial \widetilde{T}_s}{\partial t} = \nabla \cdot (\lambda_s \nabla \widetilde{T}_s) + Q. \tag{10b}$$

Across the solid–fluid interface, the fields $\{\widetilde{T}_f, \widetilde{T}_s\}$ must now satisfy:

$$\widetilde{T}_f = \widetilde{T}_s \tag{11}$$

and

$$\lambda_f (\nabla \widetilde{T}_f + \alpha \boldsymbol{e}_x) \cdot \boldsymbol{n}_{fs} = \lambda_s (\nabla \widetilde{T}_s + \alpha \boldsymbol{e}_x) \cdot \boldsymbol{n}_{fs}. \tag{12}$$

These conditions are directly derived from (7) and (8). It is evident from (12) that the assumed linear component of the temperature only induces transport of heat across parts of the interface that are not perpendicular to $\boldsymbol{e}_x$.

To nondimensionalize the energy equations we will select convenient scales of reference for the variables $\{c_p, \lambda, T, Q\}$. For the material properties, we select the fluid as the reference phase, such that $c_{p,\text{ref}} \equiv c_{p,f}$ and $\lambda_{\text{ref}} \equiv \lambda_f$. As for the reference temperature and volumetric heating rate, these are selected such that the constant, nondimensional value of α can conveniently be simplified to

$$\alpha^* = \frac{(1-\phi)}{\langle u^* \rangle_f}. \tag{13}$$

To realize this, we know from (9) that:

$$\alpha = \frac{(1-\phi)Q}{c_{p,f}\langle u \rangle_f} = \left(\frac{Q_{\text{ref}}}{c_{p,f} u_{\text{ref}}}\right) \frac{(1-\phi)Q^*}{\langle u^* \rangle_f} = \alpha_{\text{ref}} \alpha^*, \tag{14}$$

where $Q = Q_{\text{ref}} Q^*$. As $T^* = (\alpha_{\text{ref}} L_{\text{ref}}/T_{\text{ref}}) \alpha^* x^* + \widetilde{T}^*$, we select $\alpha_{\text{ref}} \equiv T_{\text{ref}}/L_{\text{ref}}$ such that after its substitution into (14):

$$\alpha^* = \left(\frac{L_{\text{ref}} Q_{\text{ref}}}{T_{\text{ref}} c_{p,f} u_{\text{ref}}}\right) \frac{(1-\phi)Q^*}{\langle u^* \rangle_f}. \tag{15}$$

Taking as reference $Q_{\text{ref}} \equiv Q$, such that $Q^* = 1$, and taking the dimensional term between parentheses equal to unity, yields for the choice of $T_{\text{ref}} \equiv L_{\text{ref}} Q/(c_{p,f} u_{\text{ref}})$ the desired result in (13). In dimensionless form, (10) can now be written as:

$$\frac{\partial \widetilde{T}_f^*}{\partial t^*} + \nabla^* \cdot \left(\boldsymbol{u}^* \widetilde{T}_f^*\right) = \frac{1}{\text{Re Pr}} \nabla^* \cdot \nabla^* \widetilde{T}_f^* - \alpha^* u^*, \tag{16a}$$

$$R_{c_p} \frac{\partial \widetilde{T}_s^*}{\partial t^*} = \frac{1}{\text{Re Pr}} \nabla^* \cdot \left(R_\lambda \nabla^* \widetilde{T}_s^*\right) + 1; \tag{16b}$$

where the Prandtl number is given by $\text{Pr} \equiv \nu\, c_{p,f}/\lambda_f$, and the ratio of solid-to-fluid material properties by $R_{c_p} \equiv c_{p,s}/c_{p,f}$ and $R_\lambda \equiv \lambda_s/\lambda_f$. As for the continuity of heat flux across the solid–fluid interface, its dimensionless form is given by:

$$\left(\nabla^* \widetilde{T}_f^* + \alpha^* \boldsymbol{e}_x\right) \cdot \boldsymbol{n}_{fs} = R_\lambda \left(\nabla^* \widetilde{T}_s^* + \alpha^* \boldsymbol{e}_x\right) \cdot \boldsymbol{n}_{fs}. \tag{17}$$

From (16) we infer that the *steady state* temperature fields $\{\widetilde{T}_f^*, \widetilde{T}_s^*\}$ are independent of R_{c_p}.

Using the computed velocity field from (5), we solve (16) for the steady-state temperature. The "total" temperatures $\{T_f^*, T_s^*\}$ are said to be thermally fully developed under a uniform heating rate. Given $\{T_f^*, T_s^*\}$, the heat transfer coefficient is computed by a straightforward post-processing of the temperature field. This is the topic of the following subsection.

Note that the proposed transport model is not valid in the limiting case $\text{Re} \to 0$. We apply a constant volumetric flow rate, which yields a constant average velocity $\langle u \rangle_f$. Changing the Reynolds number implies changing the kinematic viscosity of the fluid. In the limit $\text{Re} \to 0$, the viscosity $\nu \to \infty$. As a consequence, when Re approaches zero, we are dealing with an unphysical "infinite" viscosity fluid [the parameter α, through Eq. (9), remains constant as $\text{Re} \to 0$].

Many of the concepts previously discussed are analogous to those for fully-developed flow in tubes of constant cross section.

Author's personal copy

For a review of flows under constant wall heat flux or constant wall temperature we refer to Bejan (1993) and Incropera and DeWitt (1990).

2.3. Heat transfer coefficient

In a macroscopic description of heat transfer in porous media, empiricism is often applied to describe the microscopic coupling between the solid and fluid phases (Kaviany, 1995). In this approach the heat transfer coefficient appears as an effective transport parameter in a model for the net rate of interphase heat transfer. Before we demonstrate how to evaluate the heat transfer coefficient from microscopic simulations, we briefly recall its definition from a closure problem in the volume-averaged energy equations [for a more detailed treatment we refer to Kaviany (1995) and Slattery (1972)].

In general, the derivation of a macroscopic description requires averaging the corresponding microscopic equation over a relevant phase $\{\mathcal{V}_f, \mathcal{V}_s\}$ within the representative elementary volume $\mathcal{V}(\boldsymbol{x})$ of a porous medium (Kaviany, 1995; Whitaker, 1999); with $\boldsymbol{x}$ the centroid of $\mathcal{V}$. For a quantity ψ_f associated with the fluid phase, the phase volume average is defined as the integral over the fluid (Kaviany, 1995),

$$\langle\psi_f\rangle_f(\boldsymbol{x},t) \equiv \frac{1}{\mathcal{V}}\int_{\mathcal{V}_f}\psi_f \,\mathrm{d}V = \phi\langle\psi_f\rangle^f(\boldsymbol{x},t), \tag{18a}$$

where $\langle\psi_f\rangle^f$ is the *intrinsic* phase volume average and $\phi(\boldsymbol{x}) = \mathcal{V}_f/\mathcal{V}$ is the porosity. Similarly, for a quantity ψ_s associated with the solid phase, the phase volume average is

$$\langle\psi_s\rangle_s(\boldsymbol{x},t) \equiv \frac{1}{\mathcal{V}}\int_{\mathcal{V}_s}\psi_s \,\mathrm{d}V = (1-\phi)\langle\psi_s\rangle^s(\boldsymbol{x},t). \tag{18b}$$

Applying phase volume-averaging to the governing energy equations [Eq. (6)] yields after some manipulation (Kaviany, 1995):

$$c_{p,f}\frac{\partial\langle T_f\rangle_f}{\partial t} + \langle\nabla\cdot(\boldsymbol{u}c_{p,f}T_f)\rangle_f = \nabla\cdot\langle\lambda_f\nabla T_f\rangle_f + \frac{1}{\mathcal{V}}\int_{A_{sf}}\lambda_f\nabla T_f\cdot\boldsymbol{n}_{fs}\,\mathrm{d}A, \tag{19a}$$

$$c_{p,s}\frac{\partial\langle T_s\rangle_s}{\partial t} = \nabla\cdot\langle\lambda_s\nabla T_s\rangle_s + \frac{1}{\mathcal{V}}\int_{A_{sf}}\lambda_s\nabla T_s\cdot\boldsymbol{n}_{sf}\,\mathrm{d}A + (1-\phi)\mathrm{Q}; \tag{19b}$$

where we have made use of the theorem for the volume average of a divergence (Slattery, 1972; Howes and Whitaker, 1985). The integral terms in (19) represent the net rate of interphase heat transfer within $\mathcal{V}$,

$$q_{sf} \equiv \int_{A_{sf}}\lambda_f\nabla T_f\cdot\boldsymbol{n}_{fs}\,\mathrm{d}A = -\int_{A_{sf}}\lambda_s\nabla T_s\cdot\boldsymbol{n}_{sf}\,\mathrm{d}A. \tag{20}$$

The last equality holds as $\boldsymbol{n}_{fs} = -\boldsymbol{n}_{sf}$ (with $\boldsymbol{n}_{sf}$ the unit outwardly directed normal away from the solid phase), and due to the continuity of heat flux across the interface [Eq. (7)]. The value of q_{sf} is negative if there is a net stream of energy out of the fluid. As q_{sf} is expressed in terms of microscopic temperature gradients, a closure model must be sought that approximates q_{sf} using macroscopic gradients. A commonly used model involves the heat transfer coefficient, h_{sf}, as an effective transport parameter (Kaviany, 1995):

$$q_{sf} \approx h_{sf}A_{sf}(\langle T_s\rangle^s - \langle T_f\rangle^f). \tag{21}$$

The role of h_{sf} is to describe the rate at which heat is exchanged between phases. It is dependent on many system properties, including: flow conditions, material properties, and geometry (Bird et al., 2002). Its value can be computed from (21) if microscopic information is available on the distribution of temperature inside $\mathcal{V}(\boldsymbol{x})$.

We approximate the macroscopic transport of heat by limiting ourselves to periodic structures (Fig. 1b), where h_{sf} and ϕ are assumed constant in space. The value of h_{sf} is computed through (21) using the solution $\{T_f, T_s\}$ of (10). To compute $\langle T_s\rangle^s - \langle T_f\rangle^f$, the fields $\{T_f, T_s\}$ are averaged over their respective phases. The net rate of interphase heat transfer, q_{sf}, is in equilibrium with the total power output of the source term, and $q_{sf} = Q\mathcal{V}_s = Q(1-\phi)\mathcal{V}$.

To determine the dependency of h_{sf} on the properties of the system, we compute its dimensionless form, i.e., the Nusselt number (Nu), which is commonly defined using the reference scale $h_{sf,\mathrm{ref}} \equiv \lambda_f/L_{\mathrm{ref}}$ (Bejan, 1993; Incropera and DeWitt, 1990):

$$\mathrm{Nu} = \frac{h_{sf}L_{\mathrm{ref}}}{\lambda_f}. \tag{22}$$

Expressed in terms of the dimensionless variables:

$$\mathrm{Nu} = \frac{q_{sf}}{A_{sf}\left(\langle T_s\rangle^s - \langle T_f\rangle^f\right)}\frac{L_{\mathrm{ref}}}{\lambda_f} = \frac{(1-\phi)\mathcal{V}^*\mathrm{Re}\,\mathrm{Pr}}{A^*_{sf}\left(\langle T^*_s\rangle^s - \langle T^*_f\rangle^f\right)}. \tag{23}$$

Using (16), we can now determine the dependency of Nu on the Reynolds number, Prandtl number, and on the ratio of solid-to-fluid thermal conductivity R_λ.

With the description of the transport model complete, we will proceed with its solution strategy. We propose a strategy that can treat porous media with complex inner structures.

3. Solution strategy

The numerical method for solving the governing transport equations is briefly described in this section. An algorithm is developed based on a uniform Cartesian grid and a finite-volume method. For convenience, the algorithm is described using two spatial dimensions; the extension to three dimensions is straightforward.

3.1. Unified energy formulation

Before we discuss the details of the solution strategy we will, for numerical convenience, formulate the energy equations in a way that simplifies their discretization process later.

In line with (5), where a single equation of (mass and momentum) transport is valid throughout $\mathcal{V}$, we will adopt a similar formulation for the energy [Eq. (16)]:

$$r_{c_p}\frac{\partial\widetilde{T}}{\partial t} + \nabla\cdot[(1-\Gamma)\boldsymbol{u}r_{c_p}\widetilde{T}] = \frac{1}{\mathrm{Re}\,\mathrm{Pr}}\nabla\cdot\left(r_\lambda\nabla\widetilde{T}\right) - \alpha r_{c_p}(1-\Gamma)u + \Gamma, \tag{24}$$

with space-dependent material properties

$$r_{c_p}(\boldsymbol{x}) = [1-\Gamma(\boldsymbol{x})] + R_{c_p}\Gamma(\boldsymbol{x}) \tag{25a}$$

$$r_\lambda(\boldsymbol{x}) = [1-\Gamma(\boldsymbol{x})] + R_\lambda\Gamma(\boldsymbol{x}). \tag{25b}$$

For simplicity of notation we have dropped the asterisk. The temperature $T = \alpha x + \widetilde{T}$ now satisfies: $T = T_f$ for $\boldsymbol{x}\in\mathcal{V}_f$ and $T = T_s$ for $\boldsymbol{x}\in\mathcal{V}_s$. A unified formulation has the numerical advantage of using a single discretization stencil throughout the computational domain. This, coupled with a continuous grid across $\mathcal{V}$, provides a simple and elegant method for solving the governing transport equations. At the same time, it also avoids the use of complex domain decomposition strategies.

The equation proposed in (24) is in its strong form not well posed, as it is not valid on the interface A_{sf} due to a jump in the material properties. However, this equation is still convenient for implementation purposes, and we will develop a discretization

Author's personal copy

scheme that preserves the flux of energy across jumps in material properties, i.e., a scheme that is consistent with (17).

In (24), we have made use of the function $\Gamma(\boldsymbol{x})$ to identify the location of each phase in space. The inclusion of $(1-\Gamma)$ as a multiplier in the advective terms prevents "residual" advective-transport of heat in the solid domain and across its surface. In the solid domain there is a residual velocity field $|\boldsymbol{u}| \ll 1$ due to the source $\boldsymbol{f}$ (Lopez Penha et al., 2011), and as a consequence the advective terms are made to vanish completely in this domain.

3.2. Cartesian grid representation

To construct a computational domain we cover $\mathcal{V}$ with a uniform Cartesian grid (see Fig. 2a). For general domains, the grid will not be aligned with the surface of the solid bodies. To simplify the enforcement of the no-slip boundary condition on the surface, we choose to locally reshape the surface such that it coincides with the grid lines; thus forming a "pixelated" domain (see Fig. 2b). In this way, each grid cell is identified with a phase, i.e., being either a "solid cell" or a "fluid cell" (Lopez Penha et al., 2011). Several approaches can be taken to reshape the surface. We choose to determine whether a grid cell is solid or fluid by looking at its center-point value: if the center of a grid cell lies within the solid domain, the grid cell is considered solid; otherwise, it is fluid. This technique is suitable for applications involving uncertainties in the surface location and shape. For example, a realistic porous medium whose pore configuration can only be obtained using computer imaging techniques, such as X-ray computed tomography (Wildenschild et al., 2002). The available data set usually comprises of two-dimensional arrays of gray-scale pixels, representing cross-sectional cuts through the medium, and whose spatial resolution (and contrast) largely determines the "quality" of the solid surface (Wildenschild et al., 2002).

Each grid cell $\mathcal{V}_{ij} = [x_{i-1}, x_i] \times [y_{j-1}, y_j]$ in the computational domain is numbered by indices i and j which count cell vertex positions along the horizontal and vertical directions, respectively (see Fig. 3). The indices are taken from the set $i \in \{1,\ldots,n_x\}$ and $j \in \{1,\ldots,n_y\}$, and the dimensions of the rectangular cells are Δx and Δy. A staggered layout of the field variables is adopted, with the scalars $\{\tilde{p}, T\}_{ij}$ located in the cell centers and the velocity components $\{u, v\}_{ij}$ on the cell faces [we adopt the notation as in Verstappen and Veldman (2003)]. We identify grid cells according to their phase using Γ:

$$\Gamma_{ij} = \begin{cases} 0, & \text{if } \left(x_{i-\frac{1}{2}}, y_{j-\frac{1}{2}}\right) \in \mathcal{V}_f \\ 1, & \text{if } \left(x_{i-\frac{1}{2}}, y_{j-\frac{1}{2}}\right) \in \mathcal{V}_s, \end{cases} \tag{26}$$

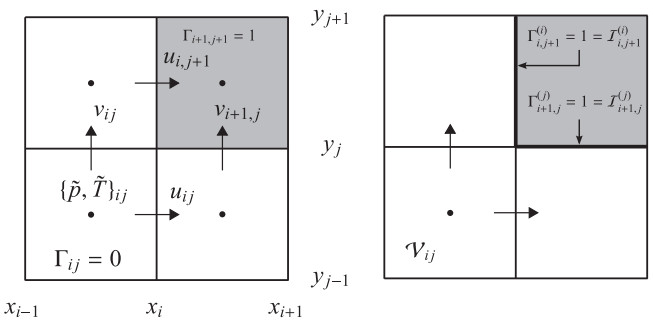

Fig. 3. Grid cells with a staggered arrangement of the field variables.

where the coordinate $(x_{i-1/2}, y_{j-1/2})$ is located at the center of cell $\mathcal{V}_{ij}$. Using Γ it is also possible to define new "functions" that identify cell faces. We will define two convenient pairs of functions (see Fig. 3). The first pair identifies cell faces, vertical and horizontal, that have on either of its sides a solid cell, i.e., for vertical faces (i = constant)

$$\Gamma^{(i)}_{ij} \equiv \max\{\Gamma_{ij}, \Gamma_{i+1\,j}\}, \tag{27a}$$

and for horizontal faces (j = constant)

$$\Gamma^{(j)}_{ij} \equiv \max\{\Gamma_{ij}, \Gamma_{i\,j+1}\}. \tag{27b}$$

It is for the faces $\{\Gamma^{(i)}, \Gamma^{(j)}\}_{ij} = 1$ that the source term $\boldsymbol{f}$ activates, and drives the velocities $\{u, v\}_{ij}$ to zero. On all other faces the source term vanishes. The second pair of functions identifies cell faces that form part of the interface A_{sf}, i.e., faces that border both a solid and a fluid cell. For the vertical and horizontal faces we define

$$\mathcal{I}^{(i)}_{ij} \equiv \begin{cases} 0, & \text{if } \Gamma_{ij} = \Gamma_{i+1\,j} \\ 1, & \text{if } \Gamma_{ij} \neq \Gamma_{i+1\,j} \end{cases} \quad \text{and} \quad \mathcal{I}^{(j)}_{ij} \equiv \begin{cases} 0, & \text{if } \Gamma_{ij} = \Gamma_{i\,j+1}, \\ 1, & \text{if } \Gamma_{ij} \neq \Gamma_{i\,j+1}, \end{cases} \tag{28}$$

respectively. With (28) we can compute an approximation to the total interfacial area:

$$A_{sf} \approx \sum_{i,j} \Delta y \mathcal{I}^{(i)}_{ij} + \Delta x \mathcal{I}^{(j)}_{ij}. \tag{29}$$

For cases where the actual geometry is aligned with the grid the value of A_{sf} is exact.

Eqs. (5) and (24) are solved using a finite-volume method and an explicit time-integrator (Lopez Penha, 2012). For integrating in time we use a second-order scheme that closely resembles the two-step Adams–Bashforth method Verstappen and Veldman

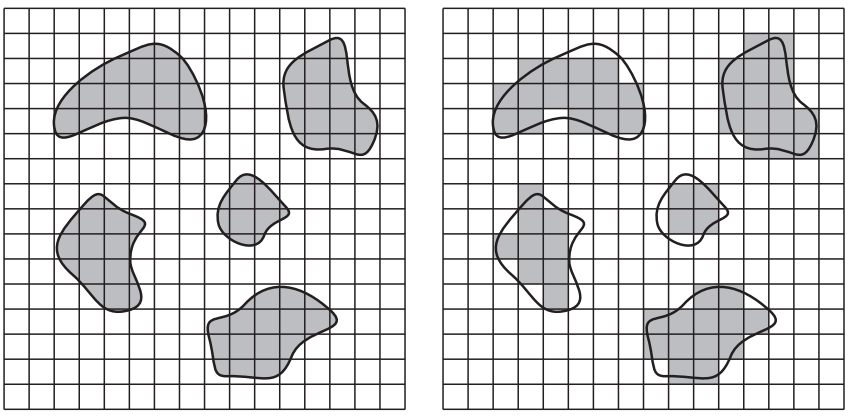

(a) REV. (b) Cartesian grid representation.

Fig. 2. Representative elementary volume $\mathcal{V}$ and its representation on a uniform Cartesian grid. Grid cells are identified as "solid cells" (colored gray) or as "fluid cells".

Author's personal copy

(2003), as this method is low-cost and has a large region of stability. To avoid excessive constraining of the time step for numerical stability, we treat the source term $\boldsymbol{f}$, in (5), in an implicit way. As for the spatial discretization, it is generally first-order accurate. Specific details concerning the discretization process can be found in Lopez Penha (2012).

4. Fully developed laminar flow in structured porous media

This section is dedicated to the simulation of fully developed laminar flow in two spatially periodic models of porous media, i.e., an inline and a staggered arrangement of square rods (see Fig. 4). These domains represent models for fibrous porous media and have been studied in great detail in Kuwahara et al. (2001), Nakayama et al. (2002, 2004), Sahraoui et al. (1994), and Kuwahara et al. (2000), where fully-developed flows have been simulated using constant wall temperature. For both porous media we will study the effects of the Reynolds number and R_λ on the Nusselt number. We also compare the results with those presented in (Kuwahara et al., 2000, 2001; Nakayama et al., 2002, 2004).

4.1. Inline arrangement of square rods

4.1.1. Limiting case of a large thermal conductivity ratio

As a basic model for a porous medium we consider an inline arrangement of infinitely extending square rods, with a cross section of the representative elementary volume $\mathcal{V}$ as illustrated in Fig. 4a. The volume $\mathcal{V}$, of dimension $H \times H \times H$, has a porosity of $\phi = 1 - (D/H)^2 = 3/4$ (taking $D = H/2$). Depth is created in $\mathcal{V}$ by extruding the cross section along the z-axis over a length H. Assume the direction of flow is along the x-axis with a constant macroscopic velocity $\langle u \rangle_f > 0$ such that the volumetric flow rate in $\mathcal{V}$ is given by $\langle u \rangle_f H^2$ (Lopez Penha et al., 2011). Taking as reference scales $L_{\text{ref}} = H$ and $u_{\text{ref}} = |\langle u \rangle_f|$, the fully-developed temperature T is completely determined by the Reynolds number, the Prandtl number and by the material properties. As for the material properties, since the volumetric heat capacity ratio R_{c_p} does not influence the steady state heat transfer, see (16), we only need to investigate the role of R_λ. This independency on R_{c_p} has been verified numerically. We consider first the limiting case of a "large" thermal conductivity ratio $R_\lambda = 10^4$, along with $\text{Pr} = 1$, and a constant volumetric flow rate such that the dimensionless velocity $\langle u \rangle_f = 1$. The value of $\alpha = (1 - \phi)/\langle u \rangle_f = 1/4$, and the Reynolds number will vary over the range $0.01 \leqslant \text{Re} \leqslant 200$. By selecting a sufficiently large R_λ we can make a direct comparison between our approach to computing the Nusselt number and that presented in Nakayama et al. (2002, 2004) for a constant wall temperature. With this choice of properties the temperature T will be uniform throughout each rod, but such that subsequent rods downstream have increasing temperatures. In a comparison between approaches we can therefore not expect the Nusselt number predictions to be similar, but like for fully-developed flow in tubes at constant heat flux or wall temperature (Bejan, 1993; Incropera and DeWitt, 1990), they are expected to be of the same order. Numerical experiments have shown that the selected value of 10^4 is an approximate lower limit for the classification of "large", as subsequent larger values have shown to have no effect on the value of the Nusselt number. We compute the temperature field T by solving for its periodic component $\widetilde{T}$ in $\mathcal{V}$ [see Eq. (24)].

We approximate $\mathcal{V}$ on a uniform Cartesian grid using three grid resolutions $n_x \times n_y \times n_z$, including: a coarse $32 \times 32 \times 4$, a medium $64 \times 64 \times 4$, and a fine $128 \times 128 \times 4$ grid. The grid spacings are $\Delta x = 1/n_x$, $\Delta y = 1/n_y$, and $\Delta z = 1/n_z$. Along the z-axis we maintain a grid resolution of $n_z = 4$ as the flow field is essentially two-dimensional, and is therefore completely independent of z. At a porosity of $\phi = 3/4$ the surface of the solid domain can always be aligned with the grid lines. For example, at a grid resolution of $32 \times 32 \times 4$, the length D can be expressed as $D = H/2 = 1/2 = \Delta x N_D$, where N_D represents the total number of grid cells spanning

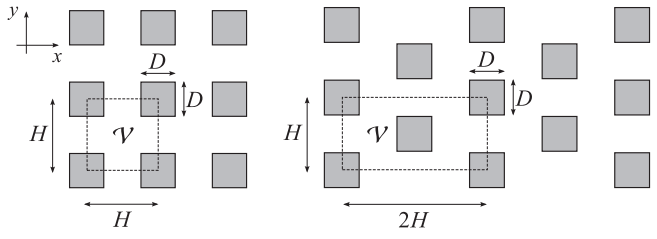

(a) Inline arrangement. (b) Staggered arrangement.

Fig. 4. Cross sections of representative elementary volumes $\mathcal{V}$ for two models of porous media. The solid squares in the (x, y)-plane are extruded along the z-axis over a length H to form a three-dimensional volume. The corner points of $\mathcal{V}$ are located at the centers of the squares.

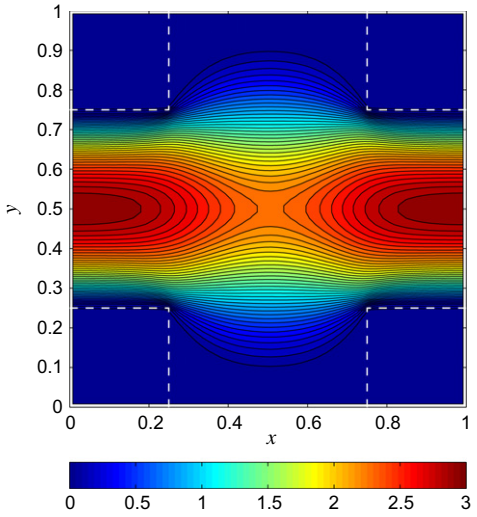

(a) Re = 1.

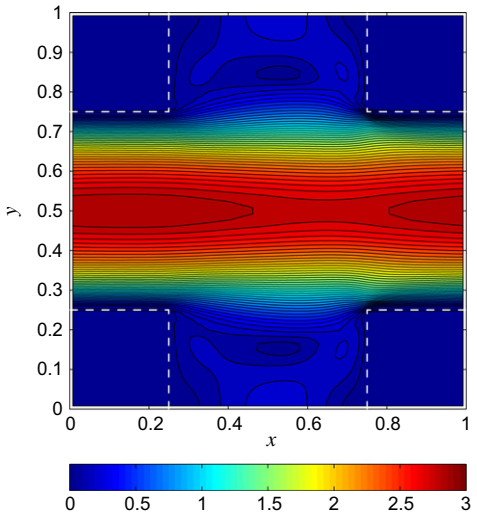

(b) Re = 100.

Fig. 5. Contour lines of fully-developed velocity magnitude $\sqrt{u^2 + v^2}$ in an inline arrangement of square rods ($\phi = 3/4$). The *dashed lines* represent the solid–fluid interface. Direction of flow is along the x-axis and the grid resolution is $n_x \times n_y = 64 \times 64$.

Author's personal copy

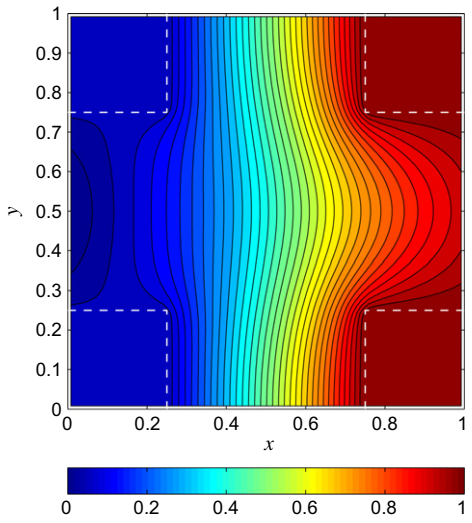

(a) Re = 1.

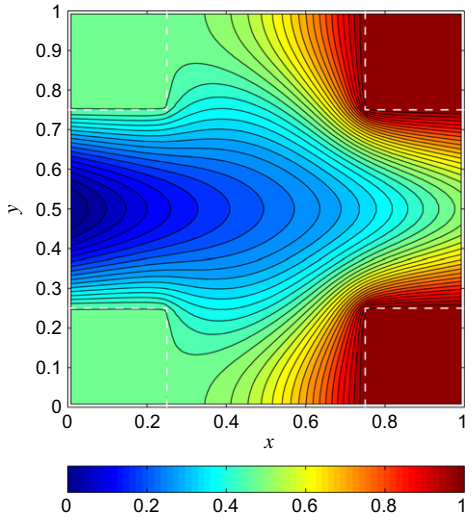

(b) Re = 10.

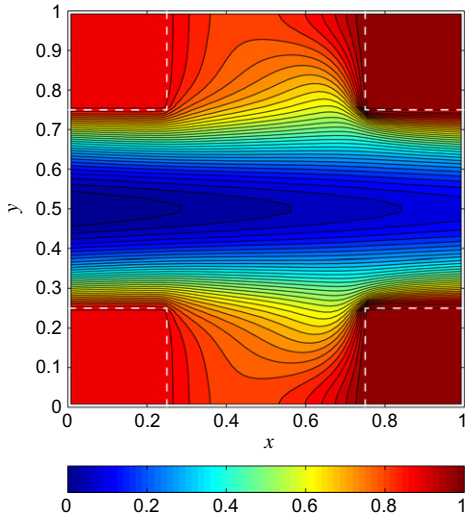

(c) Re = 100.

Fig. 6. Contour lines of fully-developed temperature T in an inline arrangement of square rods. The temperature has been transformed such that $0 \leqslant T \leqslant 1$. The porosity $\phi = 3/4$, $R_\lambda = 10^4$, and Pr = 1. Direction of flow is along the x-axis and the grid resolution is $n_x \times n_y = 64 \times 64$.

the length D. Solving for N_D gives, $N_D = 1/(2\Delta x) = n_x/2 = 16$, an integer value; therefore, setting the surface of the solid domain on the faces of grid cells.

Using the medium sized grid, we present typical results for the velocity and temperature fields $\{\boldsymbol{u}, T\}$ in Figs. 5 and 6, respectively, for the Reynolds numbers $\mathrm{Re} \in \{1, 100\}$. In Fig. 6 we also include the intermediate Re = 10. These simulations were carried out using a sufficiently small time step, $\Delta t = 5 \times 10^{-6}$, so as to maintain numerical stability and to have a negligible velocity field in the solid domain. In Fig. 5 the magnitude of velocity, $\sqrt{u^2 + v^2}$, is presented in the (x, y)-plane. The dashed lines represent the solid–fluid interface. With increasing Re the flow becomes more rectilinear and resembles Poiseuille flow between two parallel plates (Nakayama et al., 2002). The distribution of the fully-developed temperature in Fig. 6 is strongly dependent on the Reynolds number. At Re = 1 the distribution of T is relatively constant along y, whereas the distribution becomes parabolic at Re = 100 (cf. Bejan, 1993 on the distribution of T for fully-developed flow in a tube with constant heat flux). Inertial forces at Re = 1 are small, and the transport of heat by diffusion is dominant, resulting in the monotonic increase of the temperature with x. As the Reynolds number increases the advective component of transport becomes dominant and deep troughs of large temperature variation develop between the surfaces of opposing rods. For both cases of the Reynolds number we notice a uniform temperature distribution within each rod, with the downstream temperature being at a larger value. The temperature field T has been transformed such that $0 \leqslant T \leqslant 1$ in order to emphasize the areas with large relative differences in temperature.

To measure the quality of the simulated flow field we compute the Nusselt number on several refinements of the grid. Table 1 lists

Table 1
Nusselt number as a function of the Reynolds number and the spatial resolution for the inline arrangement of square rods. The porosity $\phi = 3/4$, $R_\lambda = 10^4$, and Pr = 1.

$n_x \times n_y \times n_z$	Re			
	0.1	1	10	100
$32 \times 32 \times 4$	8.14	8.18	8.91	10.63
$64 \times 64 \times 4$	8.23	8.26	8.99	10.72
$128 \times 128 \times 4$	8.26	8.29	9.03	10.75

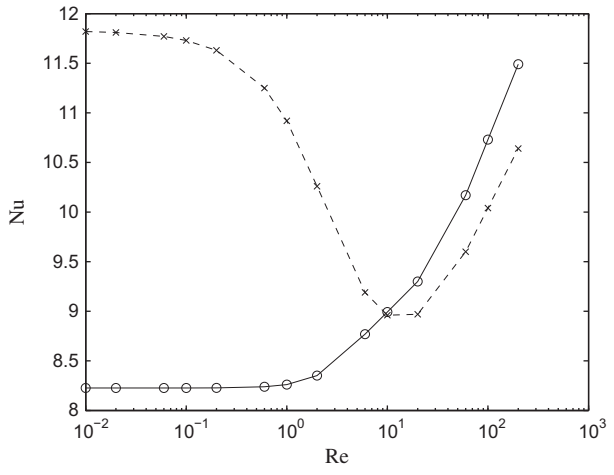

Fig. 7. Nusselt number for fully developed laminar flow in an inline arrangement of square rods as a function of the Reynolds number ($\phi = 3/4$, Pr = 1). The *solid line* represents $R_\lambda = 10^4$. All computations were carried out on the grid $n_x \times n_y = 64 \times 64$. The *dashed line* represents Nusselt numbers at constant wall temperature (Nakayama et al., 2002, 2004).

Author's personal copy

the Nusselt number as a function of the Reynolds number and the grid resolution. As the results on the medium grid are all within ~0.5% of the solution on the fine grid, we present all further results using a grid resolution in the (x, y)-plane of $n_x \times n_y = 64 \times 64$.

Fig. 7 shows the Nusselt number for a range of Reynolds numbers. The solid line represents the limiting case of a large thermal conductivity ratio, and the line increases monotonically with Re. This increase in the Nusselt number represents the increase in efficiency with which heat is extracted from the solid at higher Re. That is, compared to a small Re, a larger Re requires a smaller "driving force" ($\langle T_s \rangle^s - \langle T_f \rangle^f$) to obtain a similar rate of interphase heat transfer. Also presented in Fig. 7 are the Nusselt numbers (dashed line) for fully-developed flow at constant wall temperature, as presented in Nakayama et al. (2002, 2004). A comparison between the two lines reveals similar behavior for Re > 10 (advection dominant regime). This similarity becomes evident when we consider the distribution of the local Nusselt number along the surface of a single rod in Fig. 8c. The local Nusselt number, Nu_θ, is defined using the local heat flux at the surface (see Fig. 8a):

$$\mathrm{Nu}_\theta = \frac{-r_\lambda \nabla T \cdot \boldsymbol{n}_{sf}}{\langle T_s \rangle^s - \langle T_f \rangle^f}, \tag{30}$$

and is positive if energy is transported from the solid into the fluid. By taking the surface average of Nu_θ the Nusselt number Nu is obtained. The distribution lines of Nu_θ for Re > 10 display similar features to those presented in Kaviany (1995) and Sahraoui et al. (1994). For example, as the flow becomes more rectilinear with increasing Re the local Nusselt number increases along the top and bottom surfaces. The opposite holds true for the left and right surfaces (up-and downstream surfaces, respectively), showing a decrease in their contribution to the Nusselt number. Also noticeable is a strong contribution to the overall heat transfer by the sharp corners on the upstream side of the rod.

A large difference in behavior is seen between the lines in Fig. 7 when Re < 10, where for Re → 0 the dashed line increases before leveling off at Nu ≈ 12. This increase is attributed to the increase in the local Nusselt number along the upstream side of the rod through advection (Kaviany, 1995; Sahraoui et al., 1994). As for the solid line, a continued decrease is seen prior to its leveling at Nu ≈ 8. This behavior is attributed to the influx of energy into the solid, as is shown in Fig. 8b by the negative values of Nu_θ along the downstream side of the rod ($-90° < \theta < 90°$). The fundamental difference between the two approaches in Fig. 7 is the "applied" temperature condition along the solid–fluid interface. Under uniform heating of the solid there is a non-zero difference in temperature between rods in the streamwise direction—a difference which vanishes under constant wall temperature. It is this difference which for Re → 0 drives the transfer of heat in the upstream direction through the dominance of diffusive transport. A distinction can be made between a strongly diffusive regime Re ⩽ 0.1, where the Nusselt number is constant, and a transition regime 0.1 < Re ⩽ 10, where the Nusselt number increases rapidly due to a stronger contribution from the local velocity field to the extraction of heat.

4.1.2. Effect of varying the thermal conductivity ratio

To investigate the effect a change in the thermal conductivity ratio has on the Nusselt number, we select $R_\lambda \in \{10^0, \ldots, 10^4\}$. We limit the selected values such that $\lambda_s \geqslant \lambda_f$. By experimenting with a wide range of values for R_λ we can investigate the significance a spread in the ratio of the solid-to-fluid thermal conductivity has on the rate of interphase heat exchange. Table 2 presents the values for the Nusselt number at Re = 1. We observe that for $R_\lambda \geqslant 100$ there is almost no variation in the value of Nu. For $R_\lambda < 100$, however, a strong variation is seen, and Nu decreases

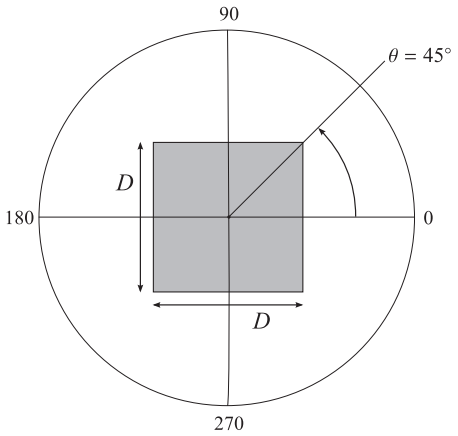

(a) Sketch representing the square rod with respect to the angular coordinate θ.

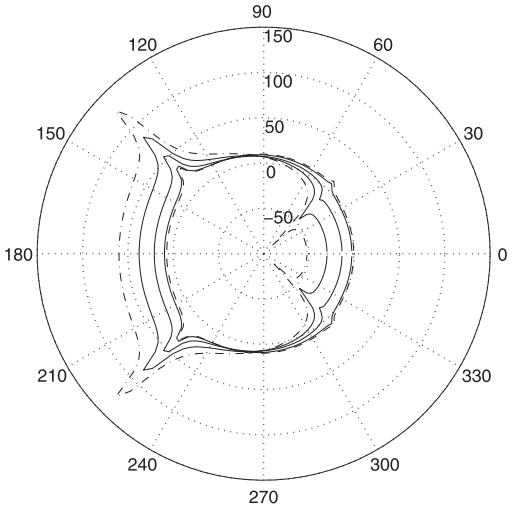

(b) Re ∈ {0.6, 1, 2, 6, 10}. *Dash-dot line*: Re = 0.6; *dashed line*: Re = 10.

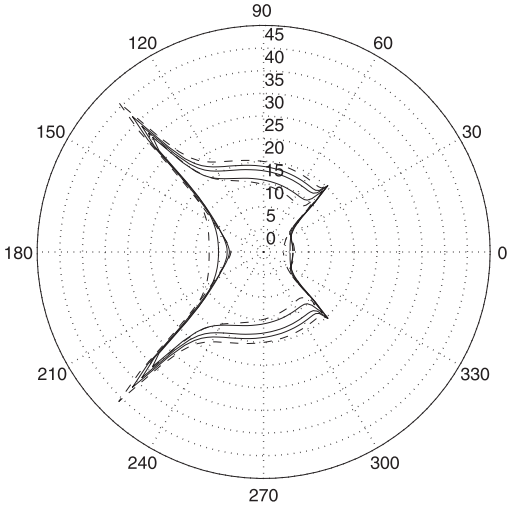

(c) Re ∈ {10, 20, 60, 100, 200}. *Dash-dot line*: Re = 10; *dashed line*: Re = 200.

Fig. 8. Polar representation of the local Nusselt number (Nu_θ) distribution on the surface of a single rod for the inline arrangement ($\phi = 3/4$, $R_\lambda = 10^4$, Pr = 1). *Dash-dot lines* represent the lowest value of Re, with subsequent lines increasing in Re up to the highest values represented with *dashed lines*.

Author's personal copy

Table 2
Nusselt number of an inline arrangement of square rods at various values of R_λ (Re = 1, Pr = 1).

	R_λ				
	10^4	10^3	10^2	10^1	10^0
Nu	8.26	8.26	8.20	7.72	5.03

with decreasing values of R_λ. We can argue for this distinction in behavior by considering the dominant physical mechanism of the system when $R_\lambda > 100$ and when $R_\lambda < 100$:

- For $R_\lambda > 100$, the thermal conductivity of the solid is much larger than that of the fluid. As energy diffuses more quickly throughout the solid, the fully-developed temperature field T_s is likely to be uniform in the interior of the domain, and a change in R_λ will unlikely alter this steady state much. Therefore, the Nusselt number is also not likely to be sensitive to a change in R_λ. Also, as a consequence of the large difference in thermal conductivities, a high rate of heat transfer develops across the solid–fluid interface due to a large thermal gradient in the fluid. The Nusselt is therefore larger than for the case when $R_\lambda < 100$.
- For $R_\lambda < 100$, the rate of conduction in the fluid is now comparable to that of the solid, and the temperature in the interior of the solid is more likely to be nonuniform. As the thermal conductivities approach the same order of magnitude, the temperature gradients across the interface diminish as the temperature field T transitions smoothly from one phase to the other. Consequently, the Nusselt number decreases with decreasing R_λ.

Table 3 presents values of Nu at Re = 100 to investigate the effect of inertia on the variation of Nu with R_λ. The behavior is similar as for the case where Re = 1, but changes in Nu are stronger with the variation in R_λ. For example, whereas for Re = 1 the relative difference between the maximum and minimum values of Nu is $(8.26 - 5.03)/5.03 \approx 64\%$, for Re = 100 this difference is $\sim 91\%$. Changing the Reynolds number has changed the dynamics of the flow field, and therefore the advective contribution to heat transfer. The contribution of inertia to the variation of Nu with R_λ is significant.

4.2. Staggered arrangement of square rods

Consider the staggered arrangement as presented in Fig. 4b, for which $\mathcal{V} = 2H \times H \times H$ (Lopez Penha et al., 2011). The porosity is constant at $\phi = 1 - (D/H)^2 = 3/4$. As reference scales we take $L_{\text{ref}} = H$ and $u_{\text{ref}} = |\langle u \rangle_f|$. Under a constant volumetric flow rate such that $\langle u \rangle_f = 1$ (implying $\alpha = 1/4$), and Pr = 1, we study the dependence of Nu on the local Reynolds number and on R_λ. The domain $\mathcal{V}$ is approximated on a uniform Cartesian grid of fixed spatial resolution $n_x \times n_y \times n_z = 128 \times 64 \times 4$.

Figs. 9 and 10 present simulation results for fully developed $\{\boldsymbol{u}, T\}$-fields at Re $\in \{1,100\}$ and $R_\lambda = 10^4$. The velocity field is quite symmetric about the $x = 1$ plane for Re = 1, whereas it becomes more complex at Re = 100 and remains symmetric only about the $y = 1/2$ plane. Fig. 10 also indicates a strong dependence of the temperature distribution on the Reynolds number. At Re = 1, the distribution across the y-axis is approximately constant in the open fluid area and parabolic, with small amplitude, between opposing horizontal walls. The distribution at Re = 100 shows strong deviations from the linear profile, $\propto x$, where deep troughs exist between opposing walls. The contours of temperature at Re = 100 largely coincide with the data in Kuwahara et al. (2000, 2001).

Table 3
Nusselt number of an inline arrangement of square rods at various values of R_λ (Re = 100, Pr = 1).

	R_λ				
	10^4	10^3	10^2	10^1	10^0
Nu	10.72	10.72	10.60	9.68	5.60

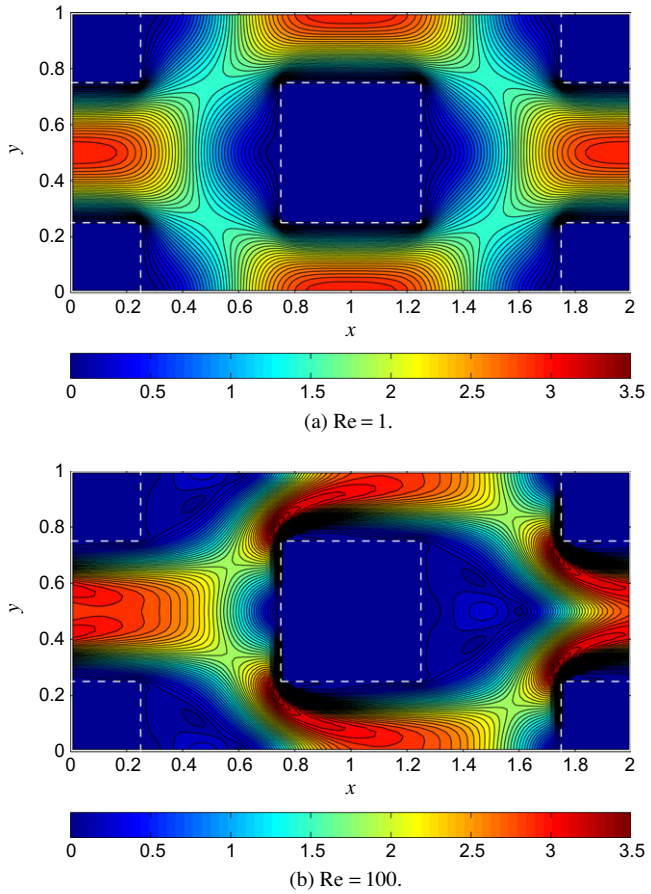

(a) Re = 1.

(b) Re = 100.

Fig. 9. Contour lines of fully-developed velocity magnitude $\sqrt{u^2 + v^2}$ in an staggered arrangement of square rods ($\phi = 3/4$). The *dashed lines* represent the solid–fluid interface. Direction of flow is along the x-axis and the grid resolution is $n_x \times n_y = 128 \times 64$.

Variations of Nu with the Reynolds number are presented in Fig. 11 for $0.01 \leqslant \text{Re} \leqslant 100$. The solid line represents the values for $R_\lambda = 10^4$. For comparison we have included values of Nu for the inline arrangement [dotted line with (○)-markers], as presented in Fig. 7. Their behavior is similar, with a constant value of Nu for $\text{Re} \leqslant 1$, and algebraic growth for $\text{Re} \gg 1$. Whereas the inline arrangement grows more quickly up to $\text{Re} \approx 10$, the staggered arrangement has a much higher growth rate for Re > 10. Also included in Fig. 11 is the graph of Nu for constant wall temperature [dashed line with (×)-markers], as presented in Kuwahara et al. (2000). Initially, its behavior as compared to the solid line is different (Re < 20). For $\text{Re} \geqslant 20$ they are almost identical. This behavior can be motivated using similar arguments as for the inline arrangement.

Table 4 presents values of the Nusselt number at Re = 1 for $R_\lambda \in \{10^0, \ldots, 10^4\}$. Similar to the inline arrangement, the Nusselt number remains approximately constant for $R_\lambda \geqslant 100$, and varies significantly for $R_\lambda < 100$.

In comparing both transport models, that for uniform heating and uniform wall temperature (Kuwahara et al., 2000, 2001;

Author's personal copy

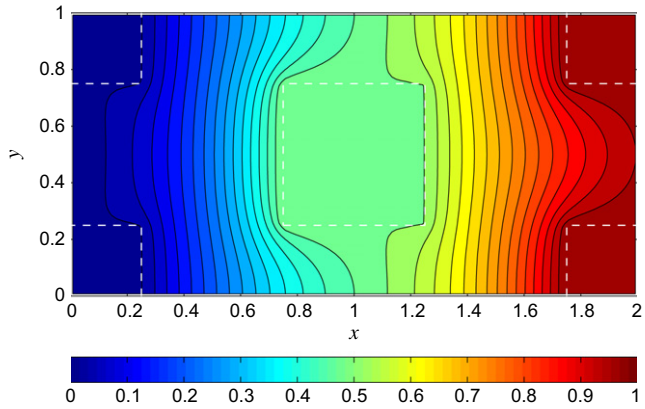

(a) Re = 1.

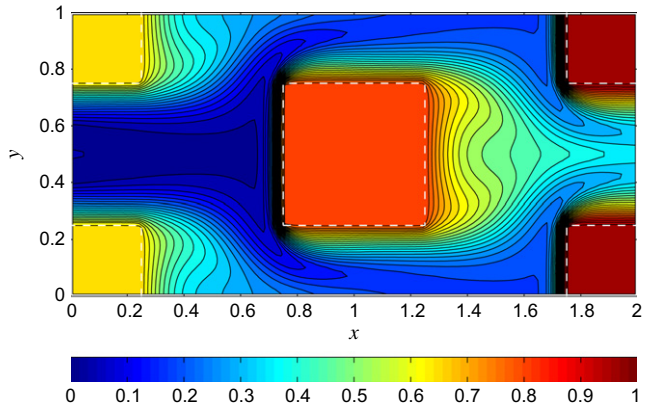

(b) Re = 100.

Fig. 10. Contour lines of fully-developed temperature T in a staggered arrangement of square rods. The temperature has been transformed such that $0 \leqslant T \leqslant 1$. The porosity $\phi = 3/4$, $R_\lambda = 10^4$, and Pr = 1. Direction of flow is along the x-axis and the grid resolution is $n_x \times n_y = 128 \times 64$.

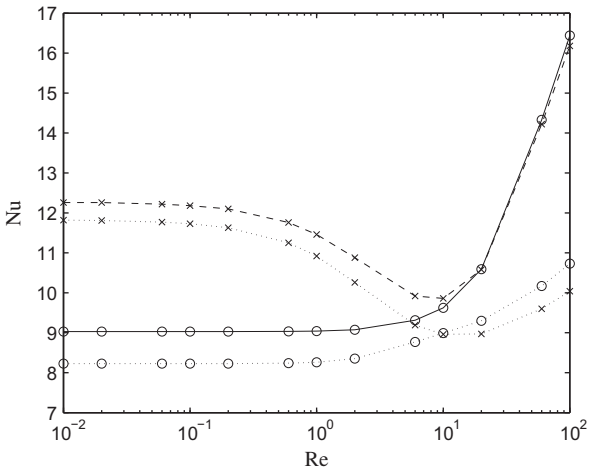

Fig. 11. Nusselt number for fully developed laminar flow in a staggered arrangement of square rods as a function of the Reynolds number ($\phi = 3/4$, Pr = 1). The (○)-markers represent $R_\lambda = 10^4$ for the inline (*dotted line*) and staggered arrangements (*solid line*). All computations were carried out on the grid $n_x \times n_y = 128 \times 64$. The (×)-markers represent Nusselt numbers at constant wall temperature for the inline (*dotted line* Nakayama et al., 2002, 2004) and staggered arrangements (*dashed line* Kuwahara et al., 2000).

Nakayama et al., 2002, 2004), we can conclude that for both the inline and staggered arrangements these models are very similar for Re $\geqslant$ 10 (inertial regime) and $R_\lambda > 100$.

Table 4
Nusselt number of a staggered arrangement of square rods at various values of R_λ (Re = 1, Pr = 1).

	R_λ				
	10^4	10^3	10^2	10^1	10^0
Nu	9.03	9.03	8.97	8.41	5.35

5. Conclusions

A computational method was developed for approximating the heat transfer coefficient of fully-developed flow in porous media. We developed a periodic transport model for incompressible fluids and conjugate heat transfer together with a numerical method for solving the model equations. The proposed method can be used as a computational aid to study the effects of pore-scale energy transport on its macroscopic behavior for cases where geometrically complex flow domains and interphase thermal coupling are important.

Fully-developed flow through porous media with uniform heating in the solid was considered. Using a periodic, representative elementary volume of the porous medium, we modeled the flow of an incompressible fluid using a volume-penalizing immersed boundary method. Volume penalization implements the no-slip condition on the surface of solid domains through a source term in the momentum equation, thereby simplifying the simulation of fluid flow in complex domains. Thermal coupling between the solid and fluid phase was realized using a unified energy formulation, allowing for advective–diffusive transport of heat in the fluid and diffusive transport with uniform heating in the solid. Using a Cartesian grid representation of the physical domain a simulation strategy was developed that is both easy to implement and utilize, as it does not require a body-conforming grid and uses a single discretization stencil. With the proposed method we were able to study the effect of system parameters on the heat transfer coefficient.

The validity and accuracy of the method was determined by performing simulations of fully developed flow in tubes of rectangular cross section with uniform wall heat flux. Accurate results were obtained for flow domains that were aligned with the grid, showing second-order convergence of the field variables. Computed Nusselt number predictions were accurate for very modest grid resolutions, with a maximum relative error of ~3% for flow in a square tube with 16×16 grid points in the cross section.

We studied the effects of various system parameters on the Nusselt number for both an inline and a staggered arrangement of square rods. For the case of a large thermal conductivity ratio $R_\lambda = 10^4$, we computed the Nusselt number as a function of the Reynolds number and compared the results with those obtained using a model for constant wall temperature (Kuwahara et al., 2000, 2001; Nakayama et al., 2002, 2004). The results agreed well for Reynolds numbers Re $\geqslant$ 10, with the inline arrangement showing a maximal difference of ~8% up to Re = 200. For the staggered arrangement, the two models were almost identical for $10 < \text{Re} \leqslant 100$. In both applications, within the inertial regime (Re $\geqslant$ 10) there was no significant difference between the two transport models on the behavior of the Nusselt number or its value. There was, however, a significant difference within the viscous regime, Re < 10. Numerical experiments performed using different values of R_λ have shown for both the inline and staggered arrangements that the Nusselt number was approximately constant for $R_\lambda \geqslant 100$ (under constant Re). For values of $R_\lambda < 100$, the Nusselt number varied significantly.

Current research is focusing on further improvements in the simulation accuracy of transport processes in complex geometries.

Author's personal copy

These improvements will generalize the applicability of the developed method to arbitrary porous media geometries (not necessarily aligned with the grid), as the current Cartesian grid representation has limitations for such cases when predicting the heat transfer properties accurately.

Acknowledgments

The authors thank Philip Morris Products S.A. for their financial support and the Netherlands National Computing Facility (NCF) for granting computing resources [performed under the NCF Project SH-061-07 with financial support from the Netherlands Organization for Scientific Research (NWO)]. The authors would also wish to thank Professor A. Nakayama and Y. Sano from Shizuoka University for providing simulation data on both the inline and staggered arrangements of square rods.

Appendix A. Deriving the value of α

To obtain a fully-developed state, the value of α is selected such that the flow of heat out of the domain $\mathcal{V}$ must balance the influx and the generation of heat in the domain. If such a balance is not satisfied, the energy of the solid and the fluid subsystems will drift, and a steady state cannot be obtained. A balance requires the time rate-of-change of the total energy in $\mathcal{V}$, i.e., E_{sf}, to vanish:

$$\frac{\mathrm{d}E_{sf}}{\mathrm{d}t} = \frac{\mathrm{d}}{\mathrm{d}t}\left(\int_{\mathcal{V}_f} c_{p,f}T_f \,\mathrm{d}V + \int_{\mathcal{V}_s} c_{p,s}T_s \,\mathrm{d}V\right) \equiv \frac{\mathrm{d}E_f}{\mathrm{d}t} + \frac{\mathrm{d}E_s}{\mathrm{d}t} = 0. \tag{A.1}$$

We express the rate-of-change of total fluid energy as follows:

$$\begin{aligned}\frac{\mathrm{d}E_f}{\mathrm{d}t} &= \int_{\mathcal{V}_f} c_{p,f}\frac{\partial}{\partial t}(\alpha x + \widetilde{T}_f)\,\mathrm{d}V = \int_{\mathcal{V}_f} c_{p,f}\frac{\partial \widetilde{T}_f}{\partial t}\,\mathrm{d}V \\ &= \int_{\mathcal{V}_f}[-\nabla\cdot(\boldsymbol{u}c_{p,f}\widetilde{T}_f) + \nabla\cdot(\lambda_f\nabla\widetilde{T}_f)]\,\mathrm{d}V - \int_{\mathcal{V}_f}\alpha u c_{p,f}\,\mathrm{d}V,\end{aligned} \tag{A.2}$$

where we have utilized (8) and the fact that in the steady state $\mathrm{d}\alpha/\mathrm{d}t = 0$. The final step was carried out through the substitution of (10a). Continuing from (A.2), we can rewrite the integrals to obtain:

$$\frac{\mathrm{d}E_f}{\mathrm{d}t} = \int_{\partial\mathcal{V}_f}[-(\boldsymbol{u}\cdot\boldsymbol{n}_{fs})c_{p,f}\widetilde{T}_f + \lambda_f\nabla\widetilde{T}_f\cdot\boldsymbol{n}_{fs}]\mathrm{d}A - \alpha c_{p,f}\langle u\rangle_f\mathcal{V}, \tag{A.3}$$

where the divergence theorem was used to convert the integral over $\mathcal{V}_f$ of the advective and diffusive terms to an integral over its surface $\partial\mathcal{V}_f$. We have also simplified the volume integral of $\alpha u c_{p,f}$ using the average velocity in $\mathcal{V}$,

$$\langle u\rangle_f = \frac{1}{\mathcal{V}}\int_{\mathcal{V}_f} u\,\mathrm{d}V. \tag{A.4}$$

In (A.3), the surface integral of $-(\boldsymbol{u}\cdot\boldsymbol{n}_{fs})c_{p,f}\widetilde{T}_f$ vanishes completely due to the periodicity of $\{\boldsymbol{u}, \widetilde{T}_f\}$ and due to the no-slip condition on the interface $A_{sf} \equiv \partial\mathcal{V}_s \cap \partial\mathcal{V}_f$. As for the integral of $\lambda_f\nabla\widetilde{T}_f\cdot\boldsymbol{n}_{fs}$, its contribution is only through the integral over A_{sf}. As a consequence, (A.3) reduces to:

$$\frac{\mathrm{d}E_f}{\mathrm{d}t} = \int_{A_{sf}}\lambda_f\nabla\widetilde{T}_f\cdot\boldsymbol{n}_{fs}\,\mathrm{d}A - \alpha c_{p,f}\langle u\rangle_f\mathcal{V}. \tag{A.5}$$

In a similar treatment, the rate-of-change of the total solid energy can be expressed as:

$$\frac{\mathrm{d}E_s}{\mathrm{d}t} = \int_{\mathcal{V}_s} c_{p,s}\frac{\partial\widetilde{T}_s}{\partial t}\,\mathrm{d}V = \int_{A_{sf}}\lambda_s\nabla\widetilde{T}_s\cdot\boldsymbol{n}_{sf}\,\mathrm{d}A + Q\mathcal{V}_s. \tag{A.6}$$

We now solve for the value of α by invoking the energy balance:

$$\frac{\mathrm{d}E_f}{\mathrm{d}t} + \frac{\mathrm{d}E_s}{\mathrm{d}t} = \int_{A_{sf}}(\lambda_f\nabla\widetilde{T}_f\cdot\boldsymbol{n}_{fs} + \lambda_s\nabla\widetilde{T}_s\cdot\boldsymbol{n}_{sf})\,\mathrm{d}A - \alpha c_{p,f}\langle u\rangle_f\mathcal{V} + Q\mathcal{V}_s = 0. \tag{A.7}$$

Simplifications can be made by noticing that:

$$\begin{aligned}\int_{A_{sf}}(\lambda_f\nabla\widetilde{T}_f\cdot\boldsymbol{n}_{fs} + \lambda_s\nabla\widetilde{T}_s\cdot\boldsymbol{n}_{sf})\,\mathrm{d}A &= \int_{A_{sf}}\alpha(\lambda_s-\lambda_f)\boldsymbol{e}_x\cdot\boldsymbol{n}_{fs}\,\mathrm{d}A \\ &= -\alpha(\lambda_s-\lambda_f)\int_{\mathcal{V}_s}\nabla\cdot\boldsymbol{e}_x\,\mathrm{d}V = 0.\end{aligned} \tag{A.8}$$

The first equality is obtained by using the continuity of heat flux at the interface [Eq. (12)] and the fact that $\boldsymbol{n}_{fs} = -\boldsymbol{n}_{sf}$. The second equality is obtained by converting the surface integral into a volume integral over $\mathcal{V}_s$ using the divergence theorem. The final integral term now vanishes by noticing that the divergence of the vector field $\boldsymbol{e}_x(\boldsymbol{x}) = (1,0,0)^T$ is zero. The value of α can now be expressed as:

$$\alpha = \frac{(1-\phi)Q}{c_{p,f}\langle u\rangle_f}, \tag{A.9}$$

where $(1-\phi) = \mathcal{V}_s/\mathcal{V}$. To maintain energy balance within $\mathcal{V}$, a balance must occur between the total rate of energy produced in the solid, $Q\mathcal{V}_s$, and the total rate of energy advected "away" from $\mathcal{V}$ by the fluid, $\alpha c_{p,f}\langle u\rangle_f\mathcal{V}$.

Appendix B. Fully developed laminar flow in rectangular tubes

To confirm the validity and accuracy of the computational model we simulate fully developed laminar flow in tubes of constant cross section. Flow in tubes of various cross sections and thermal wall boundary conditions are well documented in the literature, see for example Bejan (1993) and Incropera and DeWitt (1990). We specifically consider tubes of rectangular cross section with a constant wall heat flux in the axial (flow) direction. In case of fully-developed flow the wall temperature and bulk fluid temperature increase linearly along the tube's length (Bejan, 1993; Incropera and DeWitt, 1990). We simulate this steady state by representing a tube segment on a periodic computational domain.

Assume a computational domain $\mathcal{V} = L\times(H+2\delta_y)\times(W+2\delta_z)$ that includes the tube wall, as shown in Fig. B.12. The inner tube has a height H and width W, and L is the length of the tube segment along the x-axis. The constant wall thickness along the y and z-axis is given by δ_y and δ_z, respectively. The inclusion of a *wall domain* is a mere numerical necessity for implementing wall boundary con-

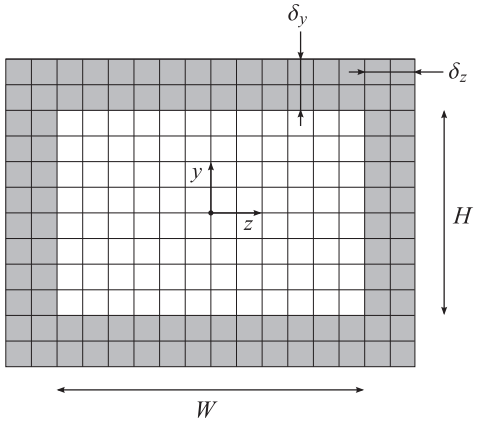

Fig. B.12. Cross section of a rectangular tube of height H and width W in the (y, z)-plane. Along the x-axis the cross section is constant. The computational domain is constructed using a Cartesian grid of uniform spacing that includes both the inner tube domain (white grid cells) and the outer wall domain (gray grid cells).

Author's personal copy

Table B.5
Effect of grid resolution on the Nusselt number Nu_D (based on the hydraulic diameter D) for fully developed laminar flow in rectangular tubes. Relative errors in % [relative to Bejan (1993) and Incropera and DeWitt (1990)] are denoted by $\Phi(Nu_D)$. The width-to-height ratios of the tubes are given by $W/H \in \{1,2,\infty\}$.

W/H	D/H	Nu_D	$\Phi(Nu_D)$ (%)	$n_x \times n_y \times n_z$
1		3.694	2.21	$4 \times 16 \times 16$
		3.625	0.30	$4 \times 32 \times 32$
		3.612	−0.06	$4 \times 64 \times 64$
	1	3.614	–	Bejan (1993)
2		4.170	1.21	$4 \times 16 \times 32$
		4.133	0.32	$4 \times 32 \times 64$
		4.125	0.12	$4 \times 64 \times 128$
	4/3	4.12	–	Incropera and DeWitt (1990)
∞		8.275	0.49	$4 \times 16 \times 4$
		8.243	0.10	$4 \times 32 \times 4$
		8.237	0.02	$4 \times 64 \times 4$
	2	8.235	–	Bejan (1993)

ditions, i.e., no-slip velocity along the inner walls of the tube and a constant wall heat flux. The actual "thickness" of this domain (in terms of grid cells) is irrelevant, and is kept to a minimum as to include more grid cells into the fluid domain. We represent $\mathcal{V}$ on a Cartesian grid of resolution $n_x \times n_y \times n_z$, with uniform spacing $\{\Delta x, \Delta y, \Delta z\}$ in each direction. The wall thickness is expressed numerically using the width of two grid cells, i.e., $\delta_y = 2\Delta y$ and $\delta_z = 2\Delta z$. The grid spacings are defined as: $\Delta x = L/n_x$, $\Delta y = H/(n_y - 4)$ and $\Delta z = W/(n_z - 4)$.

We solve the periodic transport model with the following reference scales: tube height $L_{ref} = H$ and average streamwise velocity $u_{ref} = |\langle u \rangle^f|$. To achieve a uniformly increasing temperature profile within the tube wall (Bejan, 1993; Incropera and DeWitt, 1990), i.e., where there is no variation of temperature in the wall normal direction, we select a sufficiently large thermal conductivity ratio, $R_\lambda = 10^4$. We set Re = Pr = 1, and assume a constant volumetric flow rate inside the tube such that $\langle u \rangle^f = 1$.

In Table B.5, simulation results for the Nusselt numbers are compared with reference results from literature (Bejan, 1993; Incropera and DeWitt, 1990) for three cases of the width-to-height ratio $W/H \in \{1,2,\infty\}$. For $W/H = \infty$, the flow inside the tube resembles Poiseuille flow between two parallel plates (Batchelor, 2002). The Nusselt number, Nu_D, is computed using the hydraulic diameter $D \equiv 4A_c/\mathcal{P}$ as the reference length, where A_c and $\mathcal{P}$ are the flow cross-sectional area and the wetted tube perimeter, respectively. For flow in tubes with a constant wall heat flux it is common to compute the heat transfer coefficient using the difference between the wall temperature and the bulk fluid temperature (Incropera and DeWitt, 1990). We compute Nu_D at three different spatial resolutions and quantify the accuracy of the results using the relative error. In the streamwise direction we maintain a constant resolution of $n_x = 4$, as the cross section remains constant downstream. It is evident from Table B.5 that the computed Nusselt numbers converge rapidly for tubes that are aligned with the grid. At fairly low spatial resolutions the errors are already below 3%.

References

Batchelor, G.K., 2002. An Introduction to Fluid Dynamics. Cambridge University Press, Cambridge.

Bear, J., 1988. Dynamics of Fluids in Porous Media. Dover Publications, New York.

Bejan, A., 1993. Heat Transfer. John Wiley & Sons, New York.

Bird, R.B., Stewart, W.E., Lightfoot, E.N., 2002. Transport Phenomena, second ed. John Wiley & Sons, New York.

Brenner, H., Edwards, D.A., 1993. Macrotransport Processes. Butterworth Heinemann, Boston.

Dullien, F.A.L., 1979. Porous Media: Fluid Transport and Pore Structure. Academic Press, New York.

Hinds, W.C. (Ed.), 1999. Aerosol Technology: Properties, Behavior, and Measurement of Airborne Particles, second ed. John Wiley & Sons, New York.

Howes, F.A., Whitaker, S., 1985. The spatial averaging theorem revisited. Chem. Eng. Sci. 40, 1387–1392.

Incropera, F.P., DeWitt, D.P., 1990. Fundamentals of Heat and Mass Transfer, third ed. John Wiley & Sons, New York.

Kaviany, M., 1995. Principles of Heat Transfer in Porous Media, second ed. Springer-Verlag, New York.

Kuwahara, F., Shirota, M., Nakayama, A., 2000. A numerical study of interfacial convective heat transfer coefficient in two-energy equation model of porous media. Trans. JSME 66 (645), 174–179.

Kuwahara, F., Shirota, M., Nakayama, A., 2001. A numerical study of interfacial convective heat transfer coefficient in two-energy equation model for convection in porous media. Int. J. Heat Mass Transfer 44, 1153–1159.

Lopez Penha, D.J., 2012. Simulating Microtransport in Realistic Porous Media. PhD Dissertation, University of Twente, Enschede, The Netherlands.

Lopez Penha, D.J., Geurts, B.J., Stolz, S., Nordlund, M., 2011. Computing the apparent permeability of an array of staggered square rods using volume-penalization. Comput. Fluids 51, 157–173.

Lu, D.M., Hetsroni, G., 1995. Direct numerical simulation of a turbulent open channel flow with passive heat transfer. Int. J. Heat Mass Transfer 38, 3241–3251.

Mittal, R., Iaccarino, G., 2005. Immersed boundary methods. Annu. Rev. Fluid Mech. 37, 239–261.

Moin, P., Kim, J., 1982. Numerical investigation of turbulent channel flow. J. Fluid Mech. 118, 341–377.

Nakayama, A., Kuwahara, F., Umemoto, T., Hayashi, T., 2002. Heat and fluid flow within an anisotropic porous medium. J. Heat Transfer 124, 746–753.

Nakayama, A., Kuwahara, F., Hayashi, T., 2004. Numerical modelling for three-dimensional heat and fluid flow through a bank of cylinders in yaw. J. Fluid Mech. 498, 139–159.

Quintard, M., Kaviany, M., Whitaker, S., 1997. Two-medium treatment of heat transfer in porous medium: numerical results for effective properties. Adv. Water Resour. 20, 77–94.

Sahraoui, M., Kaviany, M., 1994. Direct simulation vs volume-averaged treatment of adiabatic premixed flame in a porous medium. Int. J. Heat Mass Transfer 37, 2817–2834.

Slattery, J.C., 1972. Momentum, Energy, and Mass Transfer in Continua. McGraw-Hill, New York.

Tiselj, I., Bergant, R., Mavko, B., Bajsić, I., Hetsroni, G., 2001. DNS of turbulent heat transfer in channel flow with heat conduction in the solid wall. J. Heat Transfer 123, 849–857.

Verstappen, R.W.C.P., Veldman, A.E.P., 2003. Symmetry-preserving discretization of turbulent flow. J. Comput. Phys. 187, 343–368.

Whitaker, S., 1999. The Method of Volume Averaging. Kluwer Academic Publishers, Dordrecht.

Wildenschild, D., Vaz, C.M.P., Rivers, M.L., Rikard, D., Christensen, B.S.B., 2002. Using X-ray computed tomography in hydrology: Systems, resolutions, and limitations. J. Hydrol. 267, 285–297.